Electronic Supplementary Information

Infrared spectroscopy of live cells from a flowing solution using electrically-biased plasmonic metasurfaces

Glen Kelp[a,b,c], *Joy Li*[d], *Junlan Lu*[b], *Nicholas DiNapoli*[b], *Robert Delgado*[b], *Chao Liu*[e], *Donglei Fan*[e], *Shourya Dutta-Gupta*[b,f], *Gennady Shvets**[b]

[a] Department of Physics, University of Texas at Austin, Austin, Texas 78712, USA

[b] School of Applied and Engineering Physics, Cornell University, Ithaca, NY 14853, USA

[c] Institute of Physics, University of Tartu, Tartu, 50411, Estonia

[d] Department of Biomedical Engineering, Cornell University, Ithaca, NY 14850, USA

[e] Department of Mechanical Engineering, University of Texas at Austin, Austin, Texas 78712, USA

[f] Department of Materials Science and Metallurgical Engineering, Indian Institute of Technology Hyderabad, Hyderabad, Telangana 502285, India

* E-mail: gshvets@cornell.edu

Supplementary Text

Prior approaches to infrared spectroscopy of live cells

Several approaches to acquiring the IR spectra of live cells have been developed, as illustrated in Fig. S1. Most rely on collecting the spectra by transmitting IR light through a confluent monolayer of adherent cells. This can be done directly in transmission[1] (Fig. S1a) or using the transflection approach[2,3] (Fig. S1b), which effectively doubles the path length through the layer of cells. Such IR measurements of live cells in water solutions have been realized by injecting the cells through a shallow (~10 μm) channel between two IR transparent windows, either in transmission[4-6] (Fig. S1a) or transflection[7] (Fig. S1b) modes. Because strong water absorption in the mid-IR spectral region prevents using deeper fluidic channels for transmission-type measurements, such devices inherently suffer from low throughput. An additional limitation of transmission and transflection measurements comes from the fact that molecular information is derived from the entire cell, thus ruling out the possibility of selective interrogation of certain regions of the cell (e.g. cellular membrane), as may be desirable for specific applications.[8]

A method that alleviates some problems related to transmission spectroscopy is the attenuated total reflection (ATR) IR spectroscopy[8-10] (Fig. S1c). ATR IR spectroscopy utilizes internal reflection elements (IREs) such as prisms or hemispheres made of high refractive index materials such as silicon (Si) or germanium (Ge). Total internal reflection of the IR beam from the inner surface of such a crystal generates evanescent fields on the crystal surface that can be used to probe vibrational modes of molecules deposited on the surface. The penetration depth of the evanescent field is wavelength dependent and ranges between 0.4-1.5 μm for main biomolecule vibrational bands,[11] which is still considerably thicker than the cell membrane. Another

drawback of ATR IR spectroscopy is the relatively high cost of the IREs based on high-index crystals, thus impeding the development of single-use measurement accessories.[12]

In order to improve the sensitivity of spectroscopic measurements, various surface-enhanced techniques have been employed. Surface enhanced Raman spectroscopy (SERS) has been used for probing mid-IR vibrational modes of cells.[13,14] SERS has a number of limitations, such as long measurement times and need for sensitive detectors.[15-17] In addition, high intensity laser sources can cause photo-damage to cells.[18] Surface-enhanced IR absorption spectroscopy (SEIRAS) is another method used to measure vibrational spectra of biomolecules.[19-22]

A variant of SEIRAS is the metasurface-enhanced IR reflection spectroscopy (MEIRS, see Fig. 1a) utilized in this work. Note that the MEIRS sensor shares some similarities with surface plasmon resonance (SPR) and resonant waveguide (RWG) sensors in that it detects changes of the cellular cytoskeleton and morphology in close proximity to the sensor.[23-27] The key advantage of the MEIRS platform over the SPR/RWG platforms is that the former also contains vibrational fingerprints which can be used to ensure that the signal originates from biochemical characteristics of the cells and not from other factors (spreading, attachment, or detachment). Therefore, the MEIRS platform is potentially more “information-rich” than the more standard cell adhesion assays (either SPR or RWG) because of the specific biochemical data obtained by MEIRS-based measurements.

Supplementary Methods

Characterization of the frequency dependence of DEP force for cells

The magnitude and sign of the DEP force acting on cells is dependent on the electric field frequency and suspending medium conductivity. Before running DEP experiments with cells, it is important to know this frequency dependence for a specific cell line, in order to be able to choose the correct working frequency to attract cells onto the sensing surface. The time averaged DEP force acting on a spherical particle is given by Eq. 2 in the main text. In the 10-1000 kHz range K_{re} can be approximated to be: [28]

$$K_{re} = \frac{f^2 - {f_0}^2}{f^2 + 2{f_0}^2}, \qquad (S1)$$

where f is the frequency of applied electric field and f_0 is cross-over frequency at which DEP force is zero. It is important to note that cells are complex objects and often show considerable heterogeneity in the dielectric properties even within the same population, most notably arising from significant variety in cell radii and membrane areas which in turn affect their DEP behavior. [28-30] This results in slight variations in the cross-over frequency for individual cells.

A previously described method[31,32] employing symmetric polynomial electrode structure (Fig. S2) was chosen to characterize the frequency dependent behavior of DEP force for cells: the frequency dependent Clausius-Mossotti factor K_{re}. This method is advantageous since the electric field and its gradient (Fig. S2a) generated by such an electrode structure are relatively simple and can be described using an analytic equation: [31]

$$\left|\vec{\nabla}\left|\vec{E}\right|^2\right| = 8\left(\frac{V_2 - V_1}{2k}\right)^2 \sqrt{x^2 + y^2} = 8\left(\frac{V_2 - V_1}{2k}\right)^2 r, \qquad (S2)$$

where V_1 and V_2 are the potentials at the two electrode pairs, k is a geometric parameter (half distance between tips of hyperbola), x and y are the coordinates and r is the distance from the center of the structure. It has been shown[32] that for this configuration DEP force acting on cells is linearly dependent on the distance from the center of the structure:

$$\left|\vec{F}_{DEP}\right| = 16\pi {R_{cell}}^3 \varepsilon_s K_{re} \left(\frac{V_2 - V_1}{2k}\right)^2 r, \qquad (S3)$$

where R_{cell} is the radius of cell, ε_s is the permittivity of solution and K_{re} is real part of Clausius-Mossotti factor. This greatly simplifies data analysis.

The electrode design consists of 4 hyperbolic electrodes with the tips of the hyperbola separated by d = 260 μm (Fig. S2), corresponding to k = 130 μm. The electrode structures were fabricated from commercially available ITO on glass substrates. Details about electrode fabrication are given in Supplementary Methods section "Device fabrication for measuring cells frequency dependent DEP force".

Frequency dependence of DEP force for A431 and HCT 116 cells was determined through the measurement of K_{re}. Cells were suspended in DEP solution as described in Experimental section in the main text. Microfluidic channels made of PDMS were used to deliver cells to the electrodes. Cell movement data was recorded with Olympus IX73 inverted microscope and Panasonic DMC-GH4 video camera at 90 frames per second. Two opposing ITO electrodes were connected to one signal output of a function generator (33522B, Keysight Technologies) and the other two electrodes were connected to a second output that had π out of phase voltage signal (V_1 and V_2 on Fig. S2a). Sinusoidal voltage signal was used. Cell movement was captured at 21 different frequencies in the range 10-2000 kHz at 10 V_{pp} and 14 V_{pp}.

Quantity proportional to Clausius-Mossotti factor K_{re} was extracted by analyzing the movement of cells between the hyperbolic electrodes. Due to the symmetry of the electrodes, the cells move radially inward or outward with respect to the center point of the structure. Cell coordinates at each time instance were extracted from the videos using tracking algorithms in Adobe After Effects CC 2015. From these, cell distance from the center point of the structure r and speed u were calculated. Cell radii were calculated from visual images using a custom made MATLAB script.

It can be shown[32] that for the conditions present in this experiment, after integration of equation of motion for the cell, its velocity will be proportional to DEP force:

$$u = \frac{\left|\vec{F}_{DEP}\right|}{6\pi R_{cell}\eta}, \qquad (S4)$$

where η is the viscosity of the solution (water in this case). Combining Eq. S3 and S4 yields that velocity of a cell at any point is proportional to its distance from the electrode structure center r:

$$u = C \cdot r, \qquad (S5)$$

where C is a constant for a particular cell:

$$C = \frac{8\varepsilon_s}{3\eta}\left(\frac{V_2 - V_1}{2k}\right)^2 R_{cell}^2 K_{re}, \qquad (S6)$$

Constant C can be normalized to eliminate explicit dependence on electrode geometry, applied potential ($V_{1,2} = \pm V/2$) and cell radius:

$$C_{norm} = \left(\frac{k}{VR_{cell}}\right)^2 C = \frac{8\varepsilon_s}{3\eta} K_{re}. \qquad (S7)$$

Quantity C_{norm} now depends on suspending medium properties and K_{re}. C is obtained from experimental data ($C = u/r$), as well as R_{cell}, V and k. One value of C was calculated for each measured cell trajectory by averaging instantaneous C values over the whole trajectory. Multiple cell trajectories were found for each frequency. K_{re} can be further approximated by Eq. S1. Cross-over frequency for a particular cell line was found by fitting the frequency dependent experimentally found C_{norm} values with a curve:

$$C_{norm} = a \cdot \frac{f^2 - {f_0}^2}{f^2 + 2{f_0}^2}, \qquad (S8)$$

where a is a free parameter and f_0 is the sought after cross-over frequency.

Frequency dependent K_{re} curves calculated using experimentally determined f_0 values for HCT 116 and A431 cell lines are shown on Fig. S3. The cross-over frequency was found to be 111±24 kHz for HCT 116 and 86±20 kHz for A431. It is important to emphasize that the conductivity of the solution in these experiments was kept constant (σ_s = 781.3±1.1 μS/cm), because the curves on Fig. S3 and hence the cross-over frequency and DEP force at specific frequency are dependent on the solution conductivity.

Device fabrication for measuring frequency dependence of DEP force acting on cells

Commercial ITO on glass substrates (25×25 mm, cat. no. 703192, Sigma-Aldrich) were used to fabricate polynomial electrodes for cell frequency dependent DEP force measurements. Electrodes were created by wet etching ITO using photoresist as etch mask. Microposit S1818 photoresist (Shipley) was spin coated onto ITO at 3000 rpm for 60 s. A chrome mask carrying the electrode structure and standard photolithography methods were used to create a wet etch mask from photoresist. ITO/glass pieces were submerged in 1:1 HCl:H_2O solution for

10 minutes at room temperature to etch through the whole layer of ITO on parts of the sample not covered by photoresist. This solution was specifically chosen because of the relatively slow etch rate of ITO to minimize the etching of ITO under the photoresist near the edges of features. Samples were thoroughly washed with DI water after etching, and cleaned with acetone, IPA and DI water prior to use in experiments. The fabricated electrode structure is shown on Fig. S2b.

In order to deliver cells onto the gap between hyperbolic electrodes, PDMS microchannels were fabricated using standard soft lithography methods, as described in Experimental section ("Device fabrication") in the main text. The length of the microchannel was 16 mm, width 500 μm and height 64 μm. Polyethylene tubing (PE-20, Instech) connected the microchannel and a glass syringe holding cells in DEP solution, and the mixture was injected into the microchannel with the aid of a syringe pump. PDMS block and ITO glass with electrodes were held together using custom made acrylic clamps (Fig. S4).

Supplementary Figures

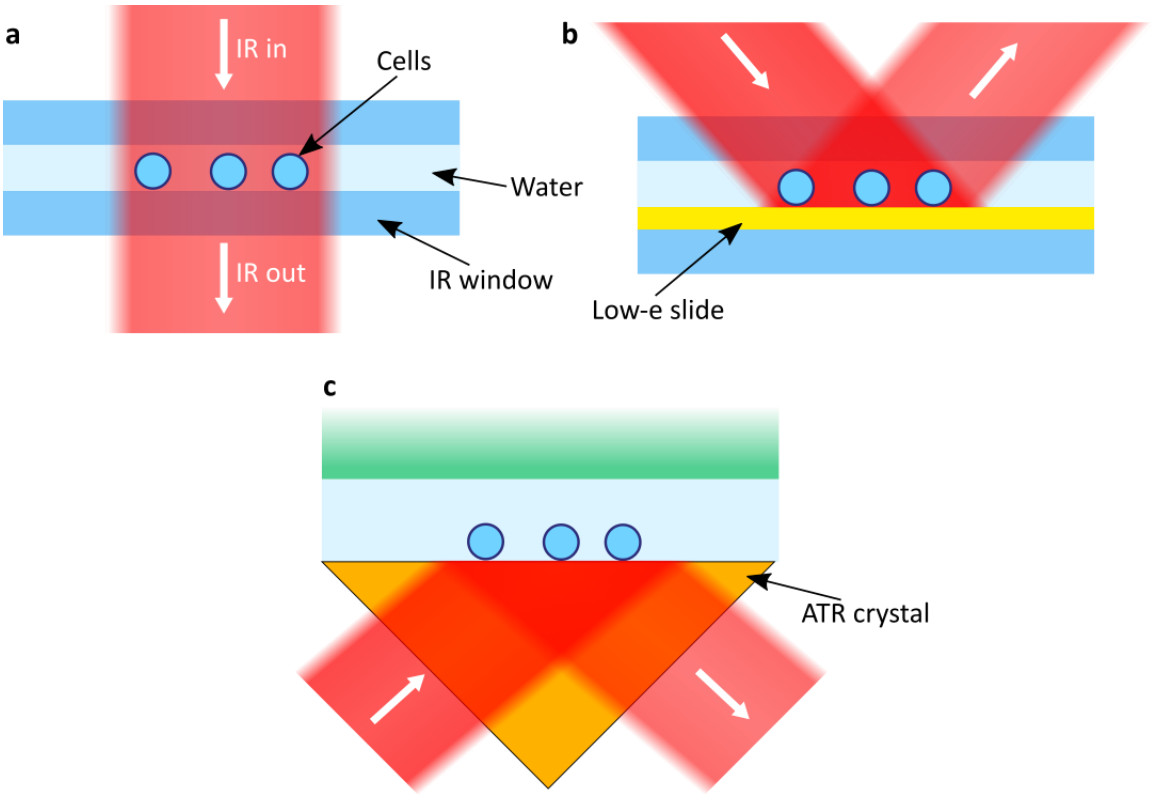

Figure S1: Methods for acquiring IR spectra of live cells in aqueous environment.

a Transmission method: the IR light is passed through cells, absorption spectra are obtained.

b Transflectance method: the light passes through the cells twice due to a reflective surface.

c ATR method: a high refractive index crystal reflects the light off the measurement surface. Due to total internal reflection, spatially localized evanescent field is generated on the measurement surface, interacting with the cells on the crystal.

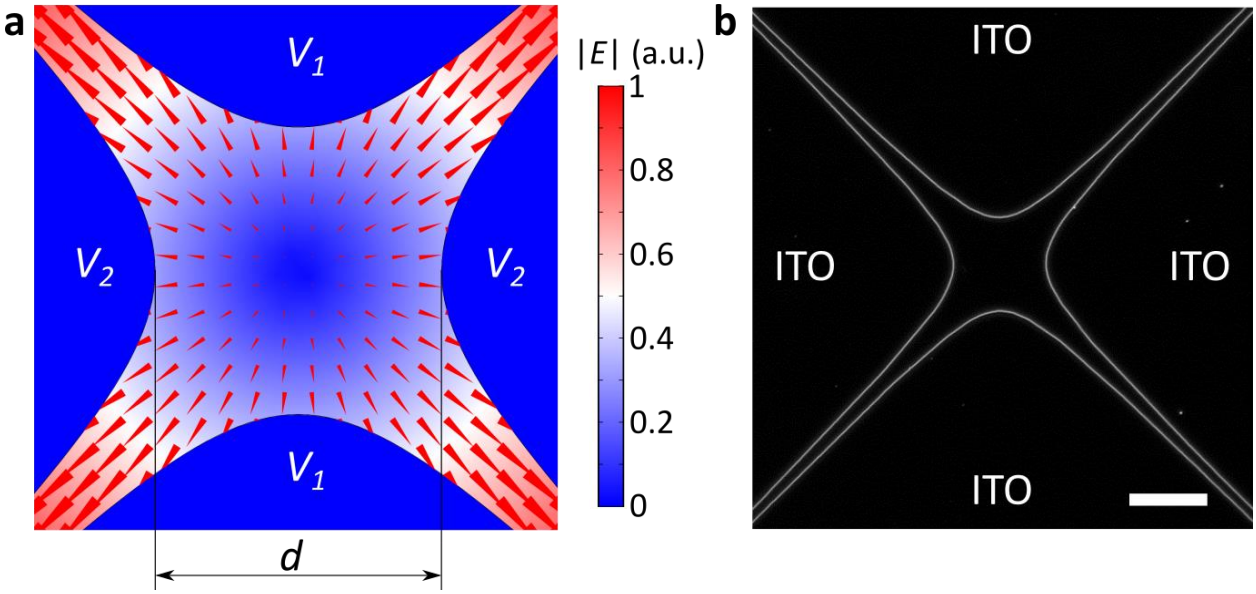

Figure S2: Hyperbolic electrodes for measuring frequency dependence of DEP force acting on cells (K_{re}). **a** Adjacent electrodes carry opposing AC voltages (V_1 and V_2 have equal amplitude, but are π out of phase). Color plot shows magnitude of electric field, and arrows show the direction and magnitude of DEP force. Tip-to-tip distance between the hyperbolic electrodes is d = 260 µm. **b** Experimentally fabricated hyperbolic ITO electrodes on glass substrate. Scale bar is 100 µm.

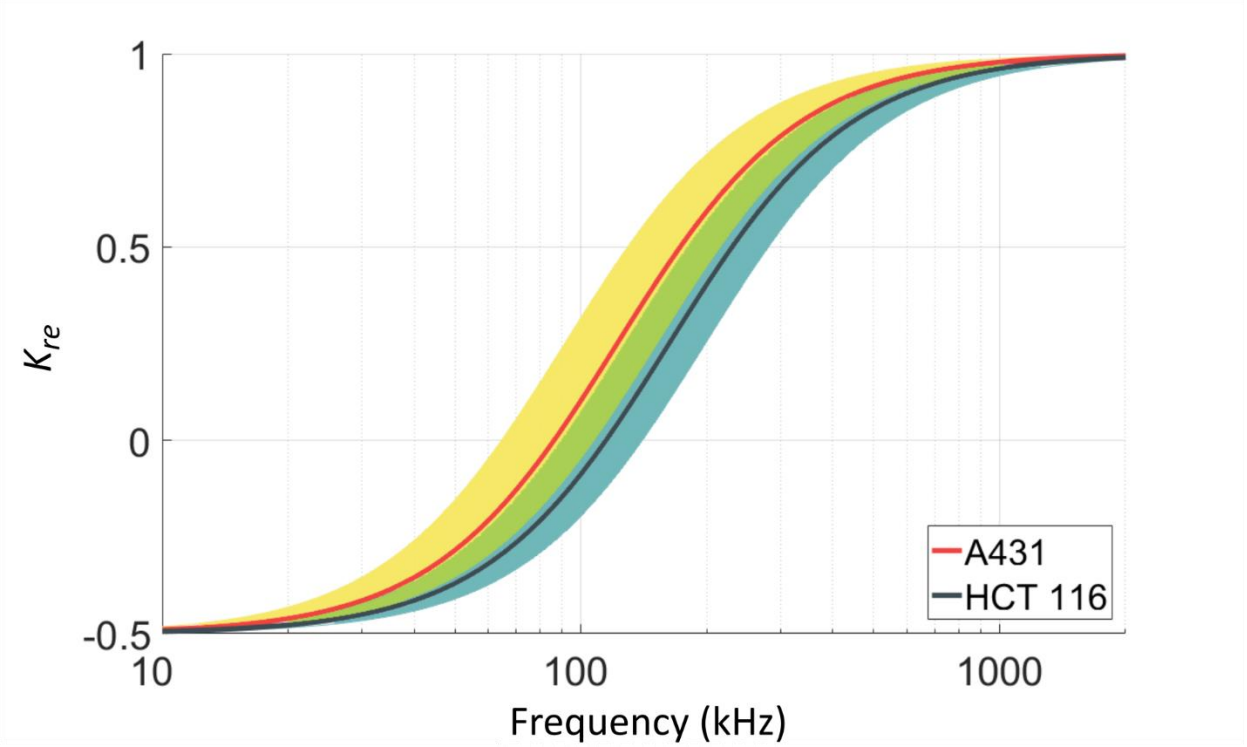

Figure S3: K_{re} curves based on experimentally determined cross-over frequency f_0 for HCT 116 and A431 cells at σ_s = 781.3±1.1 µS/cm solution conductivity. The boundaries of K_{re} curve for each cell line were obtained by using 95% confidence bounds of the fit of experimental data.

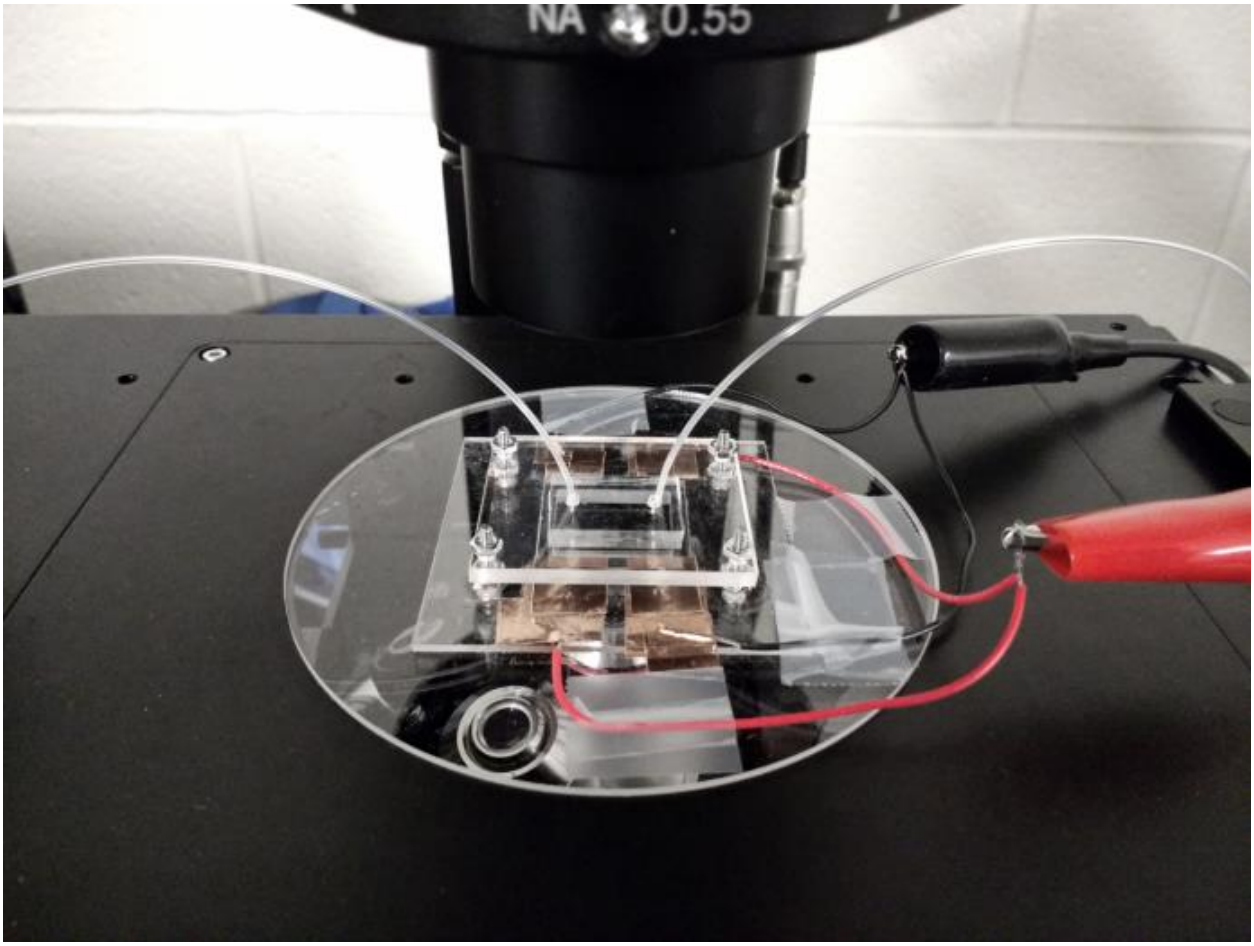

Figure S4: Device assembly for measuring frequency dependence of DEP force acting on cells. Hyperbolic ITO electrodes on glass are covered by a PDMS microfluidic channel, held together with acrylic clamps. Conductive copper tape is used to make electrical connection between the ITO electrodes and wires leading to function generator. Cells are pumped in through the tubing connected to the PDMS piece. The entire assembly is mounted on an inverted microscope.

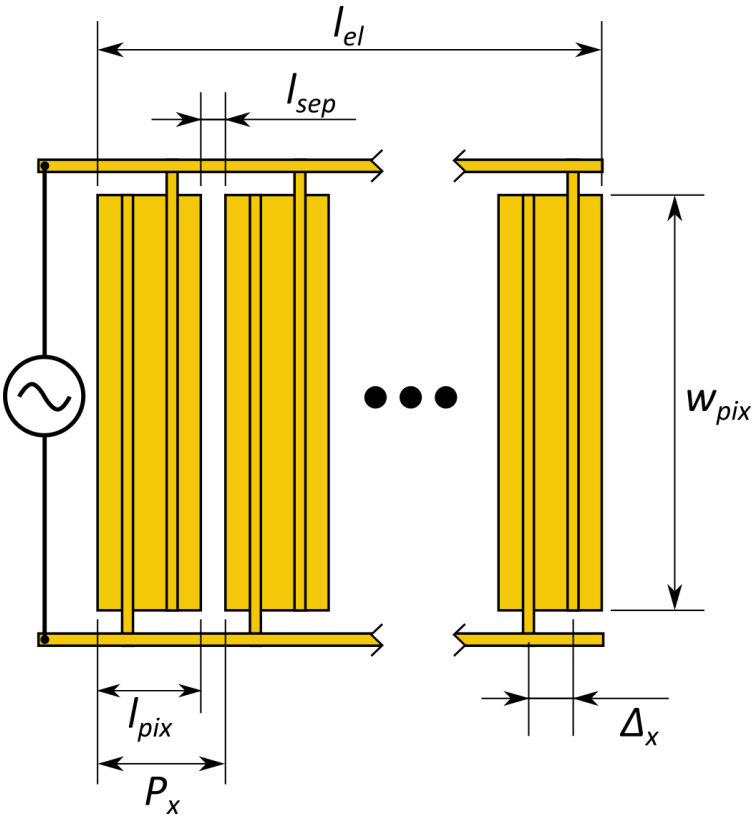

Figure S5: Dimensions of the sensing pixels. Width of each pixel is $w_{\mathrm{pix}} = 500$ µm and length $l_{\mathrm{pix}} = 120$ µm. The pixels are separated by $l_{\mathrm{sep}} = 40$ µm from each other, meaning pixel array periodicity $P_{\mathrm{x}} = 160$ µm. Two interdigitated wires separated by $\Delta_x = 40$ µm are embedded into each pixel and connected to AC voltage source. Total length of the sensing area is $l_{\mathrm{el}} \approx 2$ mm.

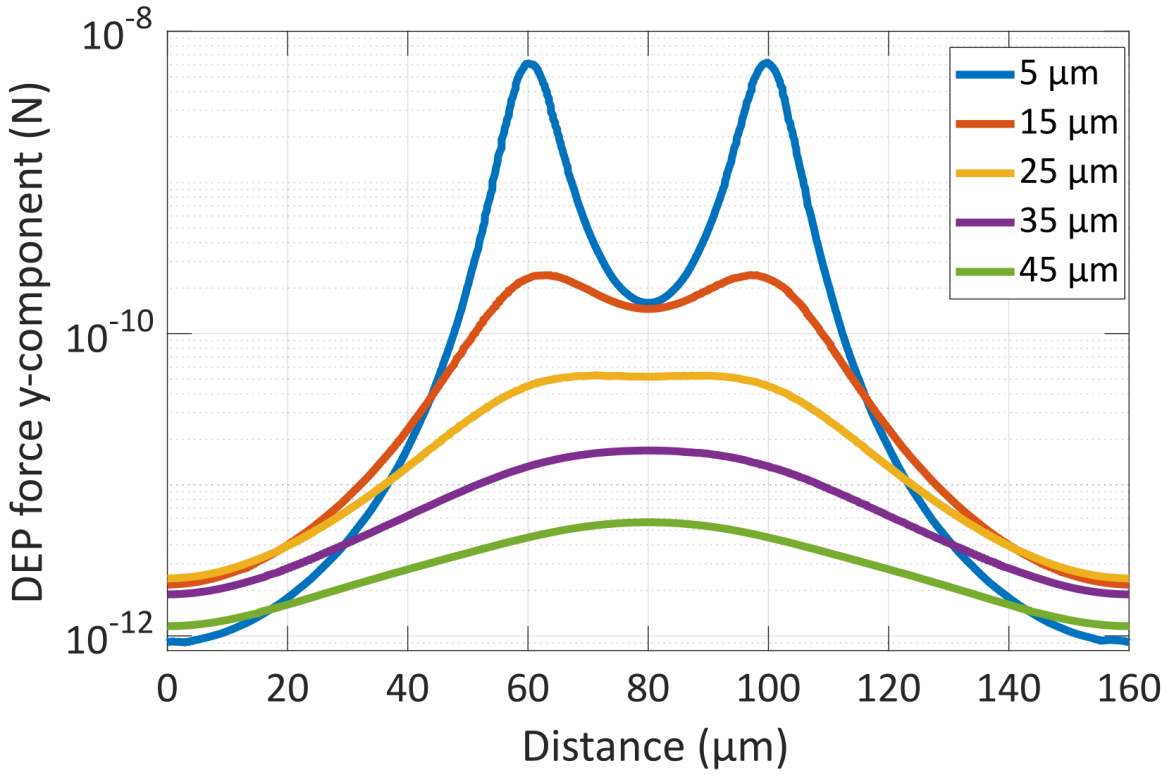

Figure S6: Magnitude of DEP force y-component over a single metasurface pixel at different distances from the metasurface (5-45 µm). Wire electrodes are located at 60 and 100 µm distance. DEP force is calculated using Eq. 2 from the main text for 14 V peak-to-peak voltage, $K_{re} = 0.8$ and $R_{cell} = 5$ µm. Sedimentation force[33] is approximately 3×10^{-13} N. Flow induced drag force on a stationary particle at 5 µm from the metasurface is 1.2×10^{-11} N, at 10 µm from the metasurface 2.3×10^{-11} N and at 15 µm from the metasurface 3.3×10^{-11} N (calculated using Eq. 5 from the main text).

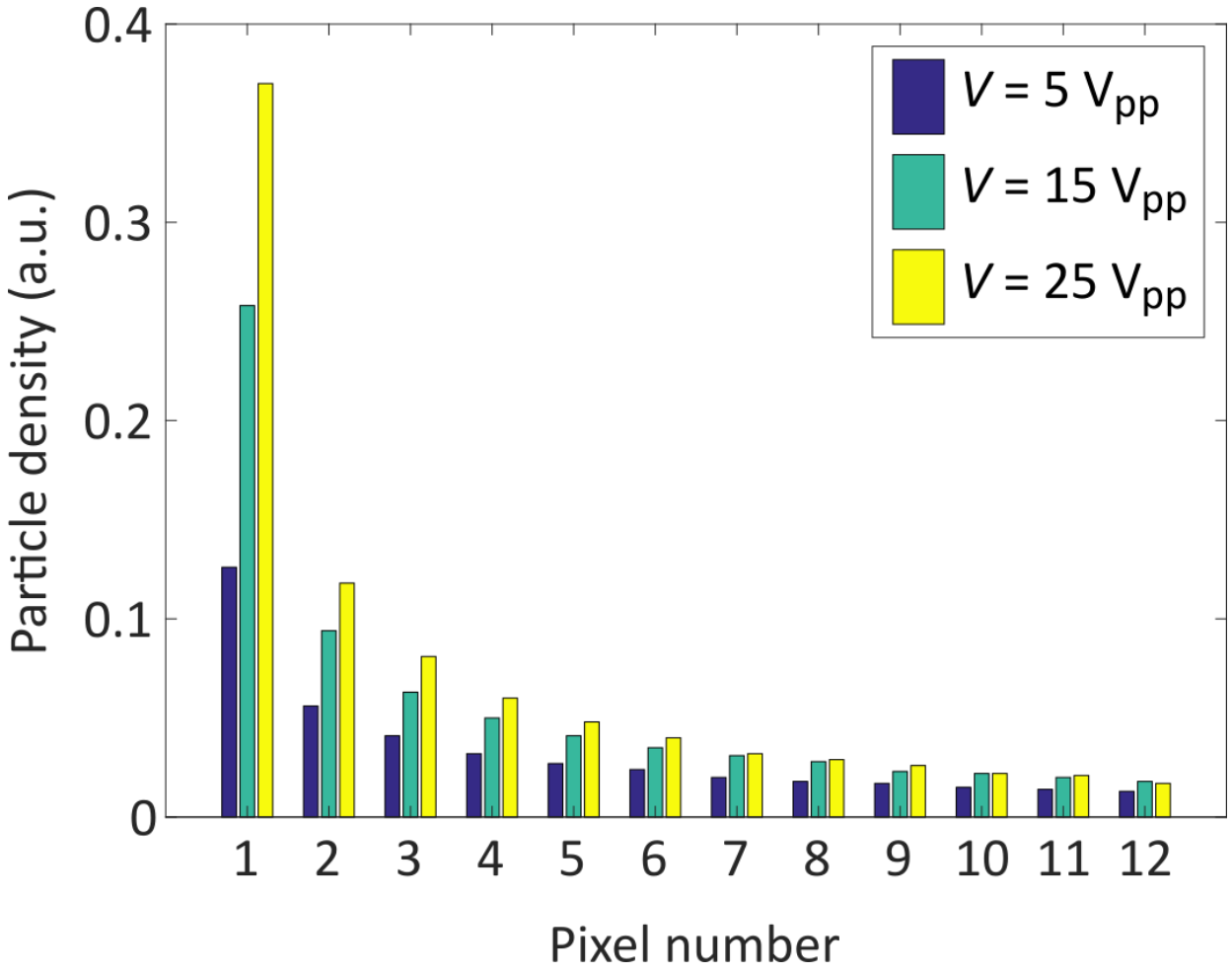

Figure S7: Numerically calculated particle density distribution on metasurface pixels. Increasing voltage yields higher number of captured particles and significantly higher density on the first few pixels closer to the microchannel inlet. Simulation parameters are as described in Experimental section in the main text, except voltages were varied (V_{pp} = 5, 15, 25 V). Flow direction is from left to right (towards increasing pixel numbers).

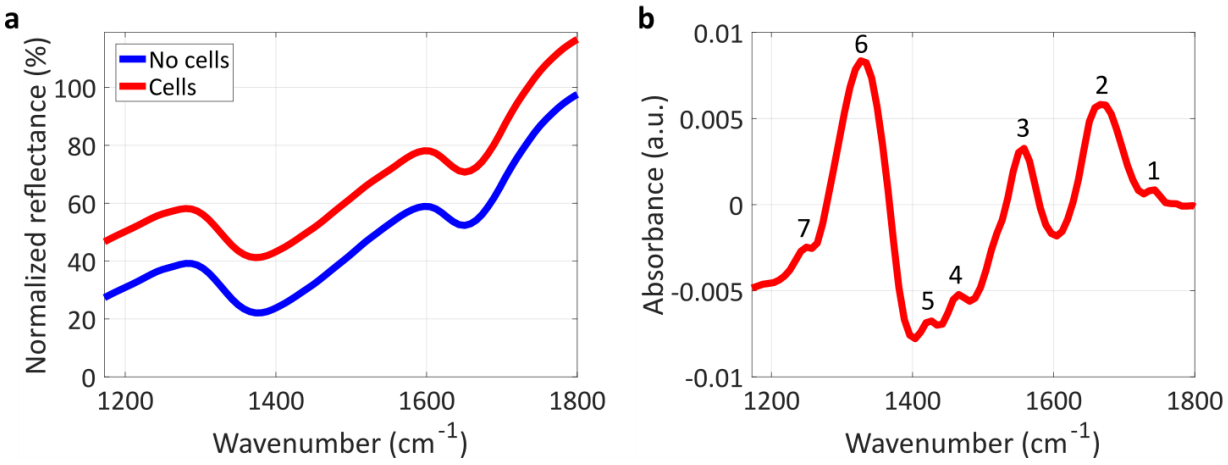

Figure S8: Example reflection and absorbance spectra of the metasurface pixel with A431 cells on it. **a** Normalized reflection spectra of the metasurface in DEP solution (blue) and after A431 cells have attached (red). Spectra are vertically shifted for clarity. **b** Absorbance spectrum calculated from spectra in **a** using Eq. 1 in the main text. The spectral features marked with numbers are listed in Table 1 in the main text.

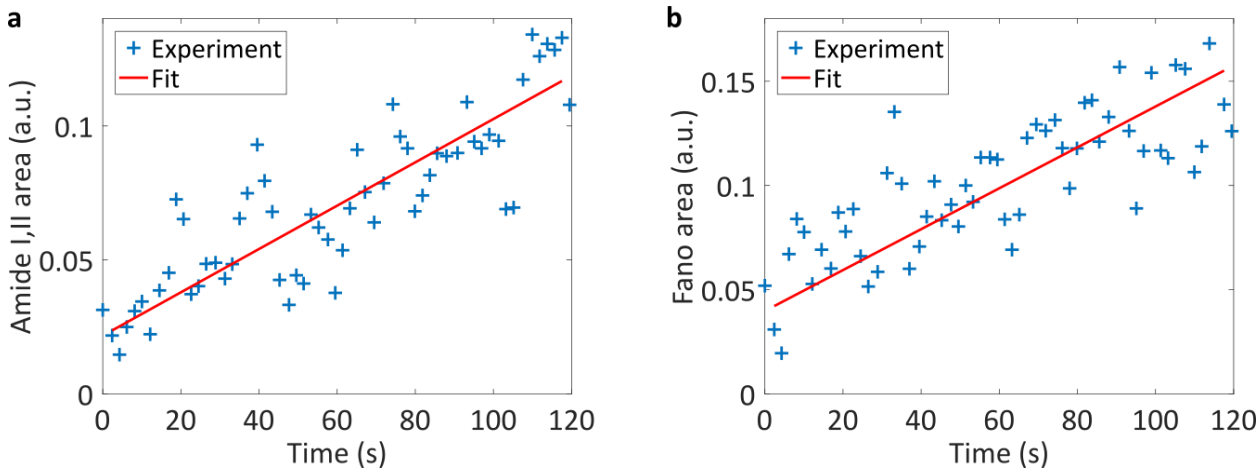

Figure S9: Control measurements to determine amide I, II and Fano feature absorbance increase associated with residual small molecules in the solution. **a** Amide I, II feature increase. **b** Fano feature increase. Red line in **a** and **b** shows a linear fit that was subtracted from time-varying absorbance feature area data collected in cell capturing and spectroscopy experiments to obtain Fig. 5b,f and 6b,c in the main text.

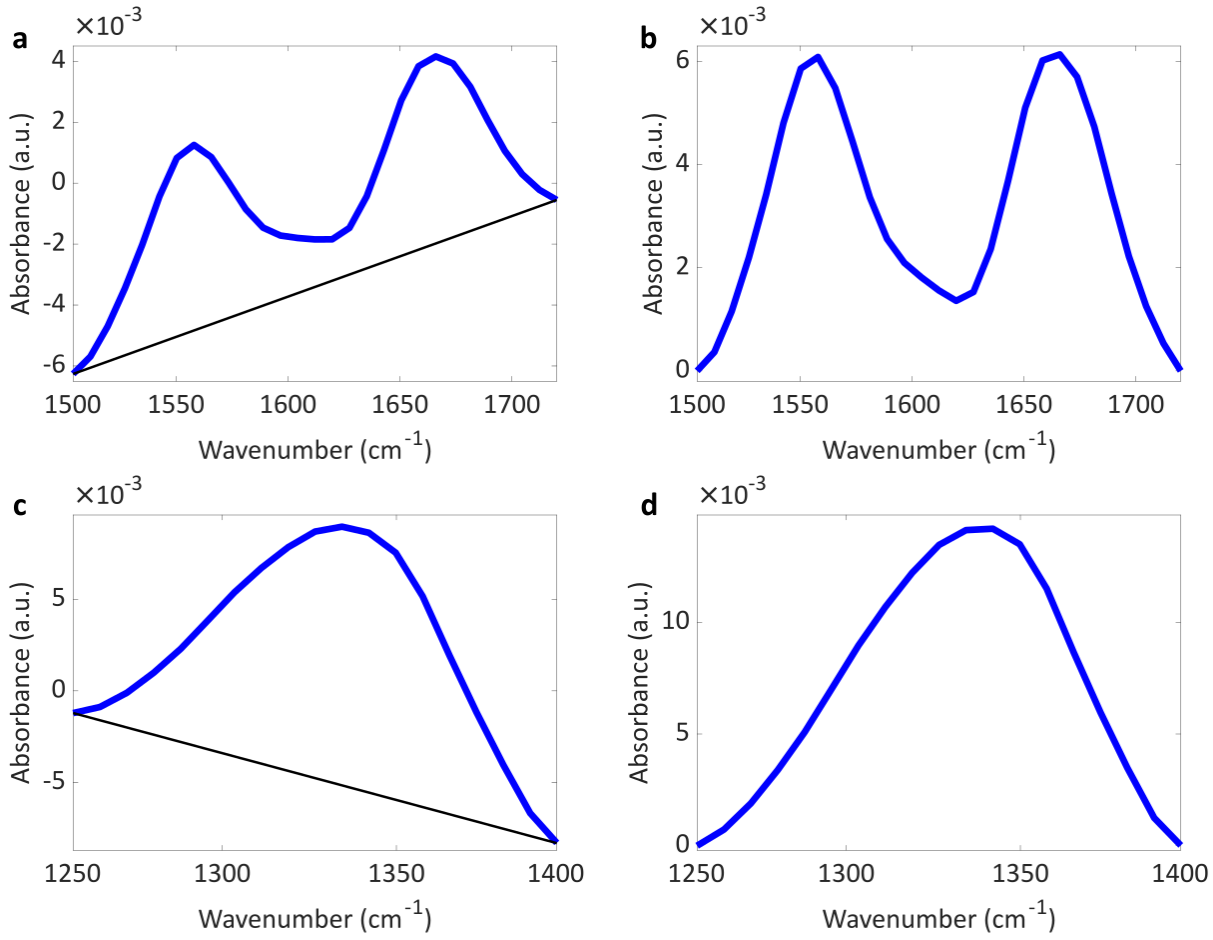

Figure S10: Examples of baseline correction of HCT 116 absorbance spectra at $t = 127$ s. **a** An example of calculated HCT 116 absorbance spectrum (blue line) in amide I and II spectral region. Linear baseline was found (black line). **b** Absorbance spectrum after subtracting the baseline shown on **a** (black line) from the calculated absorbance spectrum (blue line; also shown in Fig. 5a of the main manuscript). **c** Calculated HCT 116 absorbance spectrum (blue line) in Fano resonance feature spectral region. Linear baseline was again found (black line). **d** Absorbance spectrum after subtracting the baseline shown on **c** (black line) from the calculated absorbance spectrum (blue line; also shown in Fig. 6a of the main manuscript).

References

1. G. Bellisola and C. Sorio, "Infrared spectroscopy and microscopy in cancer research and diagnosis," *Am. J. Cancer Res.,* 2012, **2**,1.

2. M. Diem, M. Miljković, B. Bird, T. Chernenko, J. Schubert, E. Marcsisin, A. Mazur, E. Kingston, E. Zuser, K. Papamarkakis and N. Laver, "Applications of Infrared and Raman Microspectroscopy of Cells and Tissue in Medical Diagnostics: Present Status and Future Promises," *Spectroscopy,* 2012, **27**, 848360.

3. M. Miljković, B. Bird, K. Lenau, A. I. Mazur and M. Diem, "Spectral cytopathology: new aspects of data collection, manipulation and confounding effects," *Analyst,* 2013, **138**, 3975.

4. S. Kulka, N. Kaun, J. R. Baena, J. Frank, P. Svasek, D. Moss, M. J. Vellekoop and B. Lendl, "Mid-IR synchrotron radiation for molecular specific detection in microchip-based analysis systems," *Anal. Bioanal. Chem.,* 2004, **378**, 1735.

5. L. Vaccari, G. Birarda, L. Businaro, S. Pacor and G. Grenci, "Infrared Microspectroscopy of Live Cells in Microfluidic Devices (MD-IRMS): Toward a Powerful Label-Free Cell-Based Assay," *Anal. Chem.,* 2012, **84**, 4768.

6. E. Mitri, G. Birarda, L. Vaccari, S. Kenig, M. Tormen and G. Grenci, "SU-8 bonding protocol for the fabrication of microfluidic devices dedicated to FTIR microspectroscopy of live cells," *Lab Chip,* 2014, **14**, 210.

7. H.-Y. N. Holman, R. Miles, Z. Hao, E. Wozei, L. M. Anderson and H. Yang, "Real-Time Chemical Imaging of Bacterial Activity in Biofilms Using Open-Channel Microfluidics and Synchrotron FTIR Spectromicroscopy," *Anal. Chem.,* 2009, **81**, 8564.

8. J. Tittus, C. Flfili, J. K. Hilliard, J. A. Ward and A. G. U. Perera, "Early detection of cell activation events by means of attenuated total reflection Fourier transform infrared spectroscopy," *Appl. Phys. Lett.,* 2014, **104**, 243705.

9. M. Hermes, R. Brandstrup Morrish, L. Huot, L. Meng, S. Junaid, J. Tomko, G. R. Lloyd, W. T. Masselink, P. Tidemand-Lichtenberg and C. Pedersen, "Mid-IR hyperspectral imaging for label-free histopathology and cytology," *J. Opt.,* 2018, **20**, 023002.

10. S. Kazarian and K. Chan, "Applications of ATR-FTIR spectroscopic imaging to biomedical samples," *Biochim. Biophys. Acta, Biomembr.,* 2006, **1758**, 858.

11. K. L. Andrew Chan and S. G. Kazarian, "Attenuated total reflection Fourier-transform infrared (ATR-FTIR) imaging of tissues and live cells," *Chem. Soc. Rev.,* 2016, **45**, 1850.

12. K. L. A. Chan and S. G. Kazarian, "Label-free chemical detection in microfabricated devices using FT-IR spectroscopic imaging," *Spectroscopy,* 2012, **27**, 22.

13. D. I. Ellis, D. P. Cowcher, L. Ashton, S. O'Hagan and R. Goodacre, "Illuminating disease and enlightening biomedicine: Raman spectroscopy as a diagnostic tool," *Analyst,* 2013, **138**, 3871.

14. A. B. Veloso, J. P. F. Longo, L. A. Muehlmann, B. F. Tollstadius, P. E. N. Souza, R. B. Azevedo, P. C. Morais and S. W. da Silva, "SERS Investigation of Cancer Cells Treated with PDT: Quantification of Cell Survival and Follow-up," *Sci. Rep.,* 2017, **7**, 7175.

15. E. C. Faria and P. Gardner, "Single-Cell Analysis," in *Methods Mol. Biol.*, Humana Press, 2012, 151.

16. H. Byrne, G. Sockalingum and N. Stone, *Biomedical Applications of Synchrotron Infrared Microspectroscopy*, The Royal Society of Chemistry, 2011.

17. W. E. Huang, L. Mengqui, R. M. Jarvis and R. Goodacre, "Shining Light on the Microbial World: The Application of Raman Microspectroscopy," *Adv. Appl. Microbiol.,* 2010, **70**, 153.

18. J. W. Chan and D. K. Lieu, "Label-free biochemical characterization of stem cells using vibrational spectroscopy," *J. Biophoton.,* 2009, **2**, 656.

19. K. Ataka, S. T. Stripp and J. Heberle, "Surface-enhanced infrared absorption spectroscopy (SEIRAS) to probe monolayers of membrane proteins," *Biochim. Biophys. Acta, Biomembr.,* 2013, **1828**, 2283.

20. G. I. Dovbeshko, V. I. Chegel, N. Y. Gridina, O. P. Repnytska, Y. M. Shirshov, V. P. Tryndiak, I. M. Todor and G. I. Solyanik, "Surface enhanced IR absorption of nucleic acids from tumor cells: FTIR reflectance study," *Biopolymers,* 2002, **67**, 470.

21. E. Zaitseva, M. Saavedra, S. Banerjee, T. P. Sakmar and R. Vogel, "SEIRA Spectroscopy on a Membrane Receptor Monolayer Using Lipoprotein Particles as Carriers," *Biophys. J.,* 2010, **99**, 2327.

22. D. Millo, P. Hildebrandt, M.-E. Pandelia, W. Lubitz and I. Zebger, "SEIRA Spectroscopy of the Electrochemical Activation of an Immobilized [NiFe] Hydrogenase under Turnover and Non-Turnover Conditions," *Angew. Chem., Int. Ed.,* 2011, **50**, 2632.

23. Y. Yanase, T. Hiragun, K. Ishii, T. Kawaguchi, T. Yanase, M. Kawai, K. Sakamoto and M. Hide, "Surface Plasmon Resonance for Cell-Based Clinical Diagnosis," *Sensors,* 2014, **14**, 4948.

24. Y. Fang, "Probing cancer signaling with resonant waveguide grating biosensors," *Expert Opin. Drug Discovery,* 2010, **5**, 1237.

25. Y. Fang, A. M. Ferrie, N. H. Fontaine, J. Mauro and J. Balakrishnan, "Resonant Waveguide Grating Biosensor for Living Cell Sensing," *Biophys. J.,* 2006, **91**, 1925.

26. W. Chen, K. D. Long, M. Lu, V. Chaudhery, H. Yu, J. S. Choi, J. Polans, Y. Zhuo, B. A. C. Harley and B. T. Cunningham, "Photonic crystal enhanced microscopy for imaging of live cell adhesion," *Analyst,* 2013, **138**, 5886.

27. B. Cunningham, P. Li, S. Schulz, B. Lin, C. Baird, J. Gerstenmaier, C. Genick, F. Wang, E. Fine and L. Laing, "Label-Free Assays on the BIND System," *J. Biomol. Screening,* 2004, **9**, 481.

28. R. P. Gascoyne and S. Shim, "Isolation of Circulating Tumor Cells by Dielectrophoresis," *Cancers,* 2014, **6**, 545.

29. P. R. C. Gascoyne, S. Shim, J. Noshari, F. F. Becker and K. Stemke-Hale, "Correlations between the dielectric properties and exterior morphology of cells revealed by dielectrophoretic field-flow fractionation," *Electrophoresis,* 2013, **34**, 1042.

30. S. Shim, K. Stemke-Hale, J. Noshari, F. F. Becker and P. R. C. Gascoyne, "Dielectrophoresis has broad applicability to marker-free isolation of tumor cells from blood by microfluidic systems," *Biomicrofluidics,* 2013, **7**, 011808.

31. Y. Huang and R. Pethig, "Electrode design for negative dielectrophoresis," *Measurement Science and Technology,* 1991, **2**, 1142.

32. Y. Huang, R. Holzel, R. Pethig and X.-B. Wang, "Differences in the AC electrodynamics of viable and non-viable yeast cells determined through," *Physics in Medicine & Biology,* 1992, **37**, 1499.

33. P. R. C. Gascoyne, "Isolation and Characterization of Cells by Dielectrophoretic," in *Field-Flow Fractionation in Biopolymer Analysis*, Springer, 2012, 255.